

Relative  $^{235}\text{U}(n, \gamma)$  and  $(n, f)$  cross sections from  $^{235}\text{U}(d, p\gamma)$  and  $(d, pf)$ 

J. M. Allmond,<sup>1</sup> L. A. Bernstein,<sup>2</sup> C. W. Beausang,<sup>1</sup> L. Phair,<sup>3</sup> D. L. Bleuel,<sup>2</sup> J. T. Harke,<sup>2</sup> J. E. Escher,<sup>2</sup> K. E. Evans,<sup>4</sup> B. L. Goldblum,<sup>4</sup> R. Hatarik,<sup>3,5</sup> H. B. Jeppesen,<sup>3</sup> S. R. Leshar,<sup>2</sup> M. A. McMahan,<sup>3</sup> J. O. Rasmussen,<sup>3</sup> N. D. Scielzo,<sup>2</sup> and M. Wiedeking<sup>2,3</sup>

<sup>1</sup>Department of Physics, University of Richmond, Virginia 23173, USA

<sup>2</sup>Lawrence Livermore National Laboratory, Livermore, California 94551, USA

<sup>3</sup>Nuclear Science Division, Lawrence Berkeley National Laboratory, Berkeley, California 94720, USA

<sup>4</sup>Department of Nuclear Engineering, University of California, Berkeley, California 94720, USA

<sup>5</sup>Department of Physics and Astronomy, Rutgers University, Piscataway, New Jersey 08854, USA

(Received 17 March 2009; published 15 May 2009)

The internal surrogate ratio method allows for the determination of an unknown cross section, such as  $(n, \gamma)$ , relative to a better-known cross section, such as  $(n, f)$ , by measuring the relative exit-channel probabilities of a surrogate reaction that proceeds through the same compound nucleus. The validity of the internal surrogate ratio method is tested by comparing the relative  $\gamma$  and fission exit-channel probabilities of a  $^{236}\text{U}^*$  compound nucleus, formed in the  $^{235}\text{U}(d, p)$  reaction, to the known  $^{235}\text{U}(n, \gamma)$  and  $(n, f)$  cross sections. A model-independent method for measuring the  $\gamma$ -channel yield is presented and used.

DOI: 10.1103/PhysRevC.79.054610

PACS number(s): 24.87.+y, 24.75.+i, 24.50.+g, 25.85.Ge

## I. INTRODUCTION

The surrogate reaction technique, first applied in 1970 [1], has recently been the subject of intensive investigation [2–13] to establish its use and accuracy. The surrogate method (absolute [1] and ratio [4]) has been employed to circumvent technical challenges presented by the fabrication of unstable radioactive targets and the production of high-flux neutron beams. The technique allows for the determination of neutron-induced cross sections on short-lived nuclei. It additionally provides a direct test and better understanding of Bohr's postulated compound nucleus (CN) model [14]. Indeed, early experiments [15] have used the same principles as the surrogate method to test the compound nucleus model, as opposed to extracting cross sections. The surrogate technique could be useful for a number of applied areas such as stockpile stewardship and advanced fuel-cycle reactor design [16].

A significant uncertainty in the use of the surrogate reaction technique lies in the spin-parity,  $J^\pi$ , population, and decay differences between the compound nuclei formed in the desired and surrogate reactions. A schematic of the  $^{236}\text{U}$  compound-nucleus energy-spin population and decay is shown in Fig. 1. If the exit-channel probabilities have a spin-parity dependence, it could limit the use of the surrogate method [2,5,8].

Previous experiments [1,3,8,17] have tested the absolute surrogate reaction technique in the actinide region and have shown good agreement between known and surrogate deduced cross sections for low-equivalent neutron energies ( $E_n = E^* - S_n$ ). However, systematic departures have been observed at higher excitation energies due to contaminants in the target [8]. The surrogate ratio method (SRM) [4], a variation of the absolute surrogate method, avoids this and other experimental difficulties by effectively canceling the largest sources of experimental uncertainty (e.g., the particle-singles yield from detecting light ions, which can have contaminants, and detector efficiency) provided the same experimental setup is used.

Previous tests of the SRM have focused on determining  $(n, f)$  cross sections and separately  $(n, \gamma)$  cross sections by using the external surrogate ratio method (ESRM). In the ESRM, the same exit-channel probability for two different compound nuclei is measured and the unknown cross section of interest is extracted relative to a known cross section. Tests of the ESRM in the actinide region have agreed to within  $\sim 5\%$  of directly measured  $(n, f)$  cross sections over a wide range of excitation energy [11].

The *internal surrogate ratio method* (ISRM), described in this article, uses a direct reaction to form a compound nucleus at a determined excitation energy. The relative exit-channel probabilities of the surrogate compound nucleus are then measured and used to determine the relative cross sections

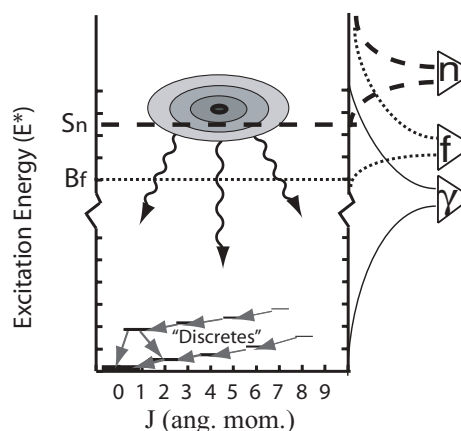


FIG. 1. A schematic of the  $^{236}\text{U}$  compound-nucleus energy-spin population (grey distribution) and decay. The exit channels open in the order of  $\gamma$  decay, fission (for  $E^* > B_f$ , where  $B_f \sim 5$  MeV is the fission barrier), and then neutron evaporation (for  $E^* > S_n$ , where  $S_n = 6.55$  MeV is the neutron-evaporation threshold). The surrogate method assumes that the exit-channel probabilities,  $P_\gamma$ ,  $P_f$ , and  $P_n$ , are the same for the desired and surrogate reactions.

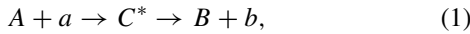
for a different entrance-channel reaction that proceeds through the same compound nucleus (e.g., neutron-induced reactions). In the present study, the  $^{235}\text{U}(d, p\gamma)$  and  $(d, pf)$  surrogate reactions are used to test the validity of the ISRM by comparing their probability ratios to the known  $^{235}\text{U}(n, \gamma)$  and  $(n, f)$  cross-section ratios.

## II. COMPOUND CROSS SECTION AND THE INTERNAL SURROGATE METHOD

Bohr's classic compound nucleus model [14] provides a simple approximation that allows a reaction to be partitioned into the following stages: formation, compound state equilibrium (CN\*), and decay. With this assumption, the decay stage becomes independent of the formation stage. This can often be realized in  $Z > 30$  nuclei [15].

A further simplification is provided by the Weisskopf-Ewing approximation [18], which eliminates the spin and parity dependence of the CN decay (constants of motion such as angular momentum and parity are still conserved however). The Weisskopf-Ewing approximation is realized when many decay channels are open for competition. This can (but not necessarily) occur when  $E^* > 2\Delta$  (where  $2\Delta$  is the pairing gap).

The compound reaction can be expressed as

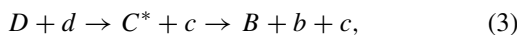


where  $A$  is the target nucleus,  $a$  is the incident projectile,  $C^*$  is the compound nucleus,  $B$  is the residual nucleus from the compound decay, and  $b$  is the final exit channel (e.g.,  $\gamma, f, xn\gamma, \dots$ ) of the compound nucleus  $C^*$ . The cross section,  $\sigma_{a,b}$ , for a reaction with entrance channel  $a$  and exit channel  $b$  can be expressed in the above limits as a product of the formation cross section,  $\sigma_a$ , and exit-channel probability,  $P_b$ ,

$$\sigma_{a,b}(E_a, E^*) = \sigma_a(E_a, E^*) \times P_b(E^*), \quad (2)$$

where  $E_a$  is the incident kinetic energy of the projectile  $a$  and  $E^*$  is the excitation energy of the compound nucleus  $C^*$ . While the incident kinetic energy,  $E_a$ , and the excitation energy,  $E^*$ , are dependent upon each other (and therefore redundant to give), both are given to recognize the need for "aligning" compound-nuclei energies when making comparisons to other (surrogate) reactions.

The surrogate (direct) reaction, which produces a highly excited nucleus that equilibrates into a compound nucleus, can be expressed as



where  $D$  is the target nucleus,  $d$  is the incident projectile,  $C^*$  is the compound nucleus,  $c$  is the particle emitted from the direct reaction  $A(a, c)C^*$  that results in the formation of the compound nucleus,  $B$  is the residual nucleus from the compound decay, and  $b$  is the final exit channel (e.g.,  $\gamma, f, xn\gamma, \dots$ ) of the compound nucleus  $C^*$ . The cross section for a reaction with entrance channel  $d$  and exit channel  $b$  can be expressed in the above (compound nucleus and Weisskopf-Ewing) limits as a product of the formation cross

section and exit-channel probability,

$$\sigma_{d,b}(E_d, E^*) = \sigma_d(E_d, E^*) \times P_b(E^*), \quad (4)$$

where  $E_d$  is the incident kinetic energy of the projectile  $d$  and  $E^*$  is the excitation energy of the compound nucleus  $C^*$ . Equations (2) and (4) are the essential components of the surrogate method and they both assume the compound nucleus and Weisskopf-Ewing approximation (see Ref. [5] for further discussion).

The ratio of cross sections for a single entrance channel,  $a$ , and two different exit channels,  $b$  and  $b'$ , can be expressed as

$$\frac{\sigma_{a,b}(E_a, E^*)}{\sigma_{a,b'}(E_a, E^*)} = \frac{P_b(E^*)}{P_{b'}(E^*)}, \quad (5)$$

because the formation cross section,  $\sigma_a(E_a, E^*)$ , is the same for all exit channels. Furthermore, the cross-section ratio, Eq. (5), is independent of the entrance channel  $a$  because the exit-channel probabilities,  $P_b$  and  $P_{b'}$ , are independent of the entrance channel (CN and Weisskopf-Ewing approximation). Therefore, the ratio of cross sections for two different entrance channels,  $a$  and  $d$ , can be equated as

$$\frac{\sigma_{a,b}(E_a, E^*)}{\sigma_{a,b'}(E_a, E^*)} = \frac{P_b(E^*)}{P_{b'}(E^*)} = \frac{\sigma_{d,b}(E_d, E^*)}{\sigma_{d,b'}(E_d, E^*)}. \quad (6)$$

Equation (6) is the *internal surrogate ratio*. This was first given by Ghoshal [15] in 1950 as a test of the Bohr compound nucleus model. However, that work compared two compound reactions as opposed to a compound reaction and a direct reaction that forms a compound nucleus.

The probability of each exit channel can be defined empirically as

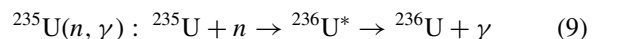
$$P_b(E^*) \equiv \frac{N_b^{C^*}(E^*)}{N^{C^*}(E^*)} \times \frac{1}{\epsilon_b}, \quad (7)$$

where  $N_b^{C^*}$  is the number of  $b$  exit-channel events observed in coincidence with a compound nucleus ( $C^*$ ),  $N^{C^*}$  is the number of compound nuclei observed, and  $\epsilon_b$  is the efficiency for detecting the  $b$  exit channel. The internal surrogate ratio can now be defined as

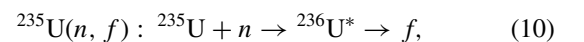
$$\frac{\sigma_{a,b}(E_a, E^*)}{\sigma_{a,b'}(E_a, E^*)} = \frac{N_b^{C^*}(E^*)}{N_{b'}^{C^*}(E^*)} \times \frac{\epsilon_{b'}}{\epsilon_b} = \frac{\sigma_{d,b}(E_d, E^*)}{\sigma_{d,b'}(E_d, E^*)}, \quad (8)$$

which is independent of the number of compound nuclei observed,  $N^{C^*}$  (i.e., particle-singles data that are often contaminated with target impurities, scattered beam, and in the present case, deuteron breakup;  $N^{C^*}$  is the largest source of systematic uncertainty in the absolute surrogate method [8]).

If the ISRM works, clearly, the cross section of a desired reaction [e.g.,  $(n, \gamma)$ ] can be determined by a surrogate reaction with Eq. (8) provided that the cross section for at least one exit channel is already known. The validity of the ISRM is tested in this work by comparing the ratio of two known cross sections,



and



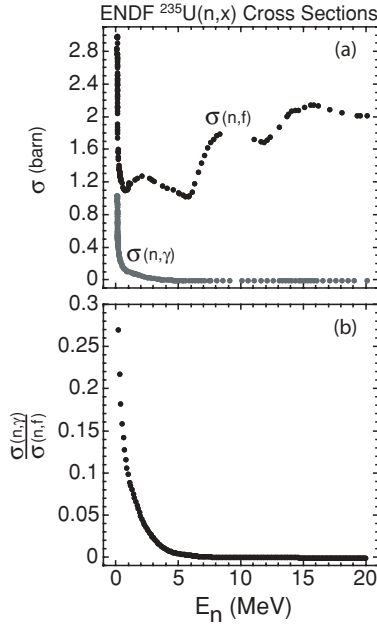


FIG. 2. (a) The known  $^{235}\text{U}(n, \gamma)$  and  $(n, f)$  cross sections from ENDF [19] ( $E_n = E^* - S_n$ ). (b) The ratio of  $^{235}\text{U}(n, \gamma)$  and  $(n, f)$  cross sections. A successful ISRM result will reproduce the ratio curve.

to the ratio of two exit-channel probabilities from the surrogate reactions,

$$^{235}\text{U}(d, p\gamma) : ^{235}\text{U} + d \rightarrow ^{236}\text{U}^* + p \rightarrow ^{236}\text{U} + \gamma + p \quad (11)$$

and

$$^{235}\text{U}(d, pf) : ^{235}\text{U} + d \rightarrow ^{236}\text{U}^* + p \rightarrow f + p. \quad (12)$$

The known  $^{235}\text{U}(n, \gamma)$  and  $(n, f)$  cross sections and their ratio, taken from ENDF [19], are shown in Fig. 2.

The choice of  $(d, p)$  as the surrogate reaction is not unique. The population of  $^{236}\text{U}$  from  $(d, p)$  should be more similar to that of neutron capture than other reactions because of the loosely bound deuteron, single-neutron transfer, low-angular-momentum transfer, minimal Coulomb excitation, and common  $^{235}\text{U}$  target. However, if a compound nucleus is truly formed, the reaction choice should not matter. Additional experiments are planned to test this assumption.

The present test of the ISRM can be expressed as

$$\frac{\sigma_{n, \gamma}(E_n, E^*)}{\sigma_{n, f}(E_n, E^*)} \Big|_{\text{ENDF}} = \frac{P_{\gamma}(E^*)}{P_f(E^*)} \Big|_{d, p} \quad (13)$$

or

$$\frac{\sigma_{n, \gamma}(E_n)}{\sigma_{n, f}(E_n)} \Big|_{\text{ENDF}} = \frac{P_{\gamma}(E_n)}{P_f(E_n)} \Big|_{d, p}, \quad (14)$$

where  $E_n = E^* - S_n$  in this scenario. Furthermore, the measured probability ratio is the  $\gamma$ -channel yield,  $^{235}\text{U}(d, p\gamma)^{236}\text{U}$ ,

divided by the fission-channel yield,  $^{235}\text{U}(d, pf)^{236}\text{U}$ ,

$$\frac{P_{\gamma}(E_n)}{P_f(E_n)} \Big|_{d, p} \equiv \frac{N_{\gamma}^{236}\text{U}(E_n)}{N_f^{236}\text{U}(E_n)} \times \frac{\epsilon_f}{\epsilon_{\gamma}} \Big|_{d, p}, \quad (15)$$

where  $N_{\gamma}^{236}\text{U}$  and  $N_f^{236}\text{U}$  are the number of  $\gamma$  and fission exit-channel events seen in coincidence with  $^{236}\text{U}$ , respectively, and  $\epsilon_{\gamma}$  and  $\epsilon_f$  are the efficiencies for detecting each exit channel, respectively. The measured components of Eq. (15) are sensitive to the methods used for tagging the exit channels. This is clarified later.

### III. EXPERIMENT

The experiment was carried out at the 88-Inch Cyclotron of the Lawrence Berkeley National Laboratory. A 21 MeV ( $\sim 1$  enA) deuteron beam was used for  $\sim 2.5$  days to produce  $^{236}\text{U}$  compound nuclei by the  $^{235}\text{U}(d, p)^{236}\text{U}$  reaction. The  $^{235}\text{U}$  target was  $450 \mu\text{g}/\text{cm}^2$  thick on a  $100 \mu\text{g}/\text{cm}^2$  carbon backing (the ISRM is insensitive to reactions on carbon).

Particle data were taken with the Silicon Telescope Array for Reaction Studies (STARS) [6] consisting of three ( $\Delta E$ ,  $E1$ , and  $E2$ ) large-area, double-sided, annular Si detectors (segmented into rings,  $\theta$ , and sectors,  $\phi$ ) configured in a  $\Delta E - E$  telescope array at forward angles  $\theta_{\text{for}} \approx 33^\circ - 41^\circ$  with respect to and symmetric about the beam axis (e.g., in azimuth,  $\phi$ ) and a single annular fission detector at backward angles  $\theta_{\text{back}} \approx 31^\circ - 62^\circ$  with respect to and symmetric about the beam axis,  $\phi$ . Coincident  $\gamma$ -ray data were collected with the Livermore-Berkeley Array for Collaborative Experiments (LIBERACE) consisting of 5 Compton-suppressed HPGe clover detectors [20] arranged in  $45^\circ$  increments within a single plane parallel to the beam axis. Figure 3 shows a schematic of the  $^{235}\text{U}$  target and detector arrangement used in the present study.

The experimental trigger required at least one of the following events: particle (i.e., a light ion through at least the first two Si detectors,  $\Delta E - E1$ , of the telescope array), particle- $\gamma$ , or particle-fission. Timing information was provided with each trigger relative to the cyclotron RF frequency ( $\sim 138.6$  ns

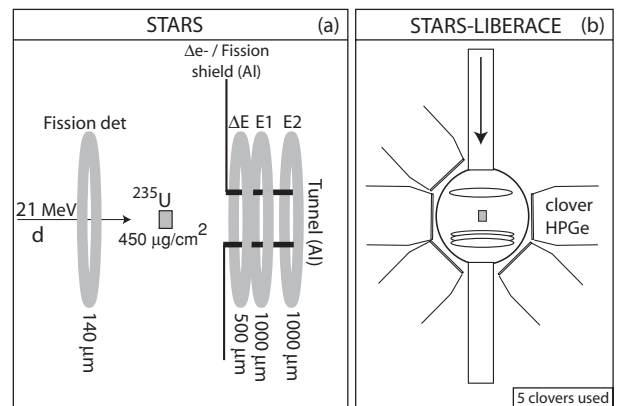


FIG. 3. (a) A schematic of the the STARS and  $^{235}\text{U}$  target arrangement used in the present study. (b) A schematic of the STARS-LIBERACE array. See text for details.

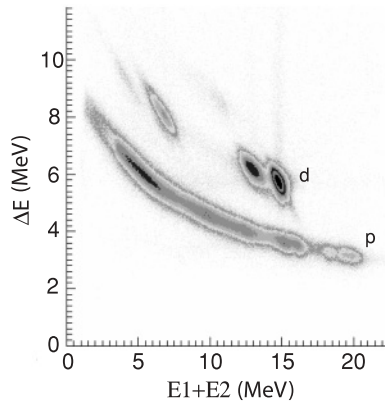


FIG. 4. A particle-identification plot showing the protons and deuterons detected by the  $\Delta E - E$  telescope array of STARS. The proton and deuteron direct-reaction exit channels are clearly differentiable.

between pulses) to differentiate between prompt and non-prompt events. Selectivity to the direct-reaction channel was achieved by the differential energy loss of the different ions in the  $\Delta E - E$  telescope (see Fig. 4). Additionally, a ray-trace (i.e., a geometric trace back to the target using the segmentation of the annular detectors) eliminated scattered beam events from the data. Each Si detector was corrected for cross-talk (induced noise) and the legitimate firing of adjacent rings (i.e., the ions can physically traverse more than one ring in a single Si detector).

The in-beam energy resolution of the  $\Delta E - E$  telescope is FWHM  $\sim 550$  keV ( $\sigma_{\text{Gaussian}} = \text{FWHM}/2.35 \sim 234$  keV) and is limited by kinematic broadening and the resolution of the third Si detector,  $E2$ , of the  $\Delta E - E$  telescope array. Energy bins of 600 keV (where a bin represents a uniform distribution with a standard deviation of  $\sigma_{\text{Uniform}} = \text{width}/3.46 \sim 173$  keV) are adopted in the particle gating to acquire sufficient statistics for the  $p-\gamma$  and  $p-f$  coincident events. This gives a total uncertainty of  $\sigma_{E^*} \sim 291$  keV in the residual-nucleus excitation energy,  $E^*$ . The relative and absolute energy calibration of the  $\Delta E - E$  telescope array is set by the following sources: (1) post-run calibrations with a  $^{226}\text{Ra}$   $\alpha$  source; (2) ( $d, d'$ ) elastic peaks of  $^{235}\text{U}$ ,  $^{12}\text{C}$ , and  $^{16}\text{O}$ ; (3) direct population of states in ( $d, p$ ) $^{13}\text{C}$  and ( $d, p$ ) $^{17}\text{O}$ ; and (4) onset of fission and neutron evaporation in the ( $d, p$ ) channel at the  $^{236}\text{U}$  fission barrier,  $B_f \sim 5$  MeV, and neutron evaporation threshold,  $S_n = 6.55$  MeV, respectively. The total

clover add-back resolution (where add-back allows for the addition of two prompt  $\gamma$  rays in adjacent segments of a HPGe clover detector [20]) at 1000 keV is FWHM  $\sim 3$  keV and the add-back singles peak efficiency at 1000 keV is  $\epsilon_{\gamma\text{-singles}} \sim 1.1\%$  (determined from a  $^{152}\text{Eu}$   $\gamma$ -ray calibration source). Further details of efficiency are discussed later.

#### IV. FISSION ANALYSIS

The total proton-gated fission spectrum from  $^{235}\text{U}(d, pf)$  is shown in Fig. 5. The heavy and light asymmetric fission fragments can be easily differentiated and there is no evidence of fission-fragment attenuation between the target and the fission detector. There is also no evidence of contaminants (e.g., backscattered light ions) in the fission spectrum (such events are eliminated by the  $p-f$  trigger and by the substantial difference in energy deposition).

The efficiency of the fission detector is taken to be the geometric efficiency (corrected for the known dead/inactive regions). Because the fissioning system produces two kinetic fragments  $\sim 180^\circ$  apart in both the center-of-mass and laboratory frame (i.e., the uranium target nucleus has little recoil), the tagging efficiency of the fission channel, cf. Eq. (15), is twice the geometric efficiency,

$$\epsilon_f = 2 \times \epsilon_{\text{geo}} = 29.2 \pm 1.4\%. \quad (16)$$

The error is dominated by a  $\pm 2$  mm uncertainty in the target-detector position. However, without  $4\pi$  coverage, departures from the geometric efficiency can occur in the event of fission-fragment anisotropy.

To investigate the effect of fission-fragment anisotropy on the fission-channel tagging efficiency, a systematic analysis was carried out and compared to past  $^{235}\text{U}(d, pf)$  experiments [21–23]. The anisotropy is reduced by the relatively large target spin of  $J^\pi = 7/2^-$  for  $^{235}\text{U}$  and low-angular-momentum transfer of  $< 3-4\hbar$  for the ( $d, p$ ) reaction. Additionally, the annular symmetry and large surface area of the STARS array coupled with near equal coverage about both  $\theta_{\text{recoil-f}} = 0^\circ$  and  $90^\circ$  (where  $\theta_{\text{recoil-f}}$  is the angle between the classical recoil axis of the residual target nucleus and fission fragment) results in little to no deviation of the fission-channel tagging efficiency from that taken by the geometry [i.e., the fission yield,  $W(\theta_{\text{recoil-f}})$ , at  $\theta_{\text{recoil-f}} = 0^\circ$  and  $90^\circ$  is  $W(0^\circ)/W(90^\circ) < 1.25$  in ratio for  $E^* > S_n$ , which integrates over the large surface area of the fission detector to give a  $< 3\%$  effect on the

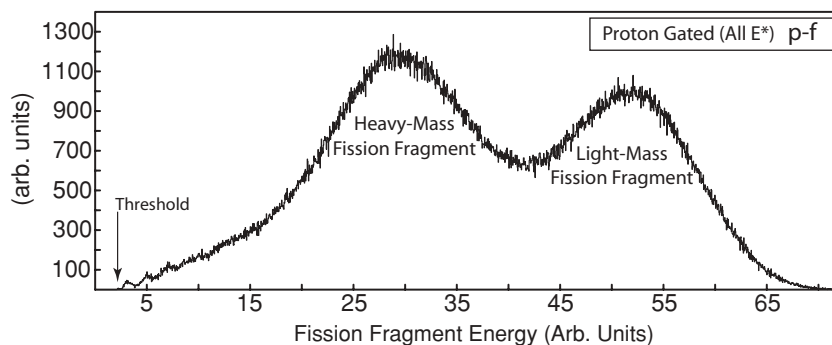


FIG. 5. The proton-gated (all) fission spectrum showing the light and heavy fission-fragment kinetic energies.

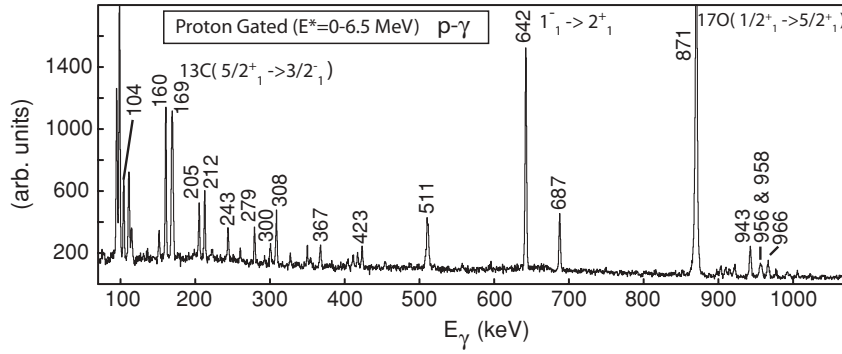


FIG. 6. The proton-gated  $\gamma$  spectrum for  $E^* \leq 6.5$  MeV. The 642 keV  $\gamma$  ray is the strongest peak from  $^{236}\text{U}$ . The carbon, 169 keV, and oxygen, 871 keV, contaminant  $\gamma$  rays come from the carbon backing and oxidation of the uranium target, respectively. These contaminants have no impact on the ISRM.

fission-channel tagging efficiency. Therefore, no correction to the fission efficiency is made with respect to anisotropy effects (i.e., negligible impact on the ISRM result compared to the geometric uncertainty of the fission detector and  $\gamma$ -ray statistics above the neutron evaporation threshold,  $S_n$ ).

## V. $\gamma$ ANALYSIS

A measure of the  $\gamma$ -channel yield,  $^{235}\text{U}(d, p\gamma)^{236}\text{U}$ , is needed to complete the probability ratio in Eq. (15). However, the  $\gamma$ -channel yield is more difficult to measure than the fission-channel yield for the following reasons: (1) germanium detectors have a relatively low photo-peak efficiency and large Compton background, (2)  $^{235}\text{U}(d, pf)$  produces a large fission-fragment  $\gamma$ -ray background, and (3)  $^{235}\text{U}(d, p\gamma)^{236}\text{U}$  for  $E^* > S_n$  has multiple  $\gamma$ -cascade paths and a relatively low cross section. Discrete  $\gamma$  transitions connecting low-energy states in  $^{236}\text{U}$  are used to identify and measure the  $\gamma$  channel.

The proton-gated,  $E^* < 6.5$  MeV,  $\gamma$  spectrum from  $^{235}\text{U}(d, p\gamma)^{236}\text{U}$  is shown in Fig. 6 and a partial level scheme for  $^{236}\text{U}$  is shown in Fig. 7. The  $J^\pi = 1^-, K^\pi = 0^-$  bandhead level at 687.6 keV serves as a strong “collector” of feeding from higher-lying states (cf. the intense 642 keV,  $1^- \rightarrow 2^+$ ,  $\gamma$  transition visible in Fig. 6). Additionally, the 642 keV  $\gamma$

transition is well isolated from background artifacts and other  $\gamma$  rays of similar energy throughout the entire energy range of interest ( $E^* < 10$  MeV), which makes it a uniquely measurable  $\gamma$  transition of  $^{236}\text{U}$ . The importance of the 642 keV  $\gamma$  ray is discussed later.

The  $\gamma$ -channel yield can be obtained by measuring the total population of the  $^{236}\text{U}$  ground state (i.e., by summing all transition intensities that directly feed the ground state). Typically, this is a nontrivial measurement for the following reasons: the level scheme could be incomplete, there could be contributions to the ground state from unobserved “side-feeding” transitions, and, in the particular case of actinide nuclei like  $^{236}\text{U}$ , the low-energy and highly converted nature of the  $2 \rightarrow 0$  yrast transition renders it impractical to observe by  $\gamma$  decay. Fortunately,  $^{236}\text{U}$  has been thoroughly studied by many different reactions and so the level scheme [24] is assumed to be complete for low energy (e.g.,  $\leq 1.5$  MeV). The remaining two concerns are addressed below.

The population of a state is defined as

$$I_{\text{tot}} = \Sigma I_{\text{out}} = \Sigma I_{\text{in-discrete}} + \Sigma I_{\text{in-unobserved}}, \quad (17)$$

where  $\Sigma I_{\text{out}}$  is the total intensity out of a state,  $\Sigma I_{\text{in-discrete}}$  is the discrete (observed) intensity feeding a state, and  $\Sigma I_{\text{in-unobserved}}$  is the unobserved intensity feeding a state (i.e., “unobserved side feeding”). Therefore, the total population of the  $^{236}\text{U}$  ground state is given by

$$I_{\text{tot}}(0^+) = \Sigma I_{\text{in-discrete}}(0^+) + \Sigma I_{\text{in-discrete}}(2^+) + \Gamma, \quad (18)$$

where  $\Sigma I_{\text{in-discrete}}(0^+)$  and  $\Sigma I_{\text{in-discrete}}(2^+)$  are the sums of the observed transition intensities directly feeding the  $0^+$  and  $2^+$  yrast states, respectively, and  $\Gamma$  is the unobserved side-feeding intensity to the  $0^+$  and  $2^+$  yrast states. The transitions to the  $2^+$  yrast state provide the substitute for the unobserved  $2 \rightarrow 0$  yrast transition. The  $\gamma$  transitions used to determine the  $\gamma$ -channel yield are labeled with an asterisk in Fig. 7.

Unfortunately, for excitation energies above the neutron evaporation threshold ( $S_n = 6.55$  MeV), the 642 keV  $\gamma$  ray (cf. Figs. 6 and 7) is the only statistically significant transition observed. Therefore, the 642 keV  $\gamma$  ray must be used to tag the  $\gamma$  channel for  $E^* > S_n = 6.55$  MeV. To use this transition to tag the  $^{235}\text{U}(d, p\gamma)^{236}\text{U}$   $\gamma$  channel, the fraction of the  $\gamma$  channel represented by the 642 keV transition must be known. Furthermore, this fraction must be independent of excitation energy  $E^*$  (or vary in a predictable manner).

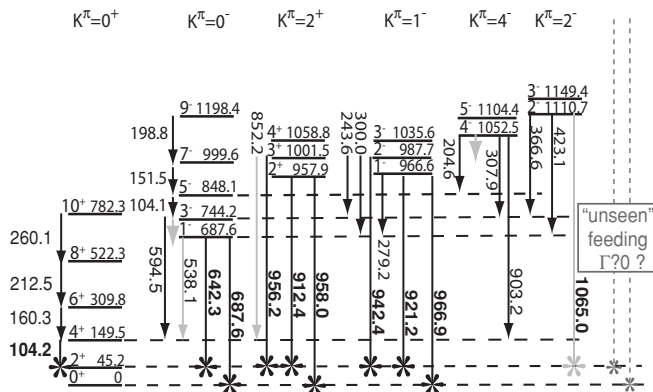


FIG. 7. A partial level scheme of  $^{236}\text{U}$  for the present  $^{235}\text{U}(d, p\gamma)^{236}\text{U}$  study. The “gray” transitions are not observed but inferred from the Nuclear Data Sheets (NDS) [24]. The conversion electrons are also inferred from the NDS. All transitions with an asterisk directly feed the  $J^\pi = 0^+$  and  $2^+$  yrast states and they are used to measure the  $\gamma$ -channel yield.

The fraction of the  $^{235}\text{U}(d, p\gamma)^{236}\text{U}$   $\gamma$  channel represented by the 642 keV transition is

$$F_{\gamma\text{-ch}}(642) = \frac{I(642)}{I_{\text{tot}}(0^+)}, \quad (19)$$

where  $I(642)$  is the discrete intensity of the 642 keV,  $1^- \rightarrow 2^+$ , transition (corrected for efficiency and internal conversion) and  $I_{\text{tot}}(0^+)$  is the  $\gamma$ -channel yield as defined in Eq. (18). Fortunately,  $I_{\text{tot}}(0^+)$  and, therefore,  $F_{\gamma\text{-ch}}(642)$ , can be determined for  $E^* < S_n$ , where the  $\gamma$  statistics are higher [cf. the drop in the  $\gamma$ -channel cross section for  $E^* > S_n$  in Fig. 2(a)]. However, two concerns must be addressed in determining the 642 keV decay fraction,  $F_{\gamma\text{-ch}}(642)$ , and its validity for  $E^* > S_n$ :

- (i) The amount of unobserved side feeding,  $\Gamma$ , that contributes to the  $\gamma$ -channel yield,  $I_{\text{tot}}(0^+)$ , must be determined.
- (ii) The 642 keV decay fraction,  $F_{\gamma\text{-ch}}(642)$ , must be shown to be constant with excitation energy,  $E^*$ .

The unobserved side-feeding intensities can be determined for a given level from the state population or intensity balance definition, Eq. (17), by a rearrangement of terms,

$$U = \Sigma I_{\text{in-unobserved}} = \Sigma I_{\text{out}} - \Sigma I_{\text{in-discrete}}. \quad (20)$$

Unobserved side-feeding intensities have been determined for several low-energy discrete states in  $^{236}\text{U}$  over an excitation energy range of  $2.6 < E^* < 6.5$  MeV. This interval is chosen to maximize the statistics of the  $\gamma$ -ray transitions and to exclude direct population of the low-energy discrete states.

The measured unobserved side-feeding distributions are plotted in Fig. 8(a) as a function of spin and the distributions are grouped by band assignment,  $K^\pi$ . As can be seen, the measured distributions for the  $K^\pi = 0^+$  yrast band and the  $K^\pi = 0^-$  negative-parity band are quite similar (i.e., they both go through a maximum at spin  $\sim 5-6\hbar$  and decrease at higher and lower spins). The distribution for the yrast band ends at  $J^\pi = 4^+$  because the  $2^+ \rightarrow 0^+$  yrast transition cannot be observed. However, the  $K^\pi = 0^-$  negative-parity band provides a measure of the unobserved side feeding down to  $J^\pi = 1^-$ . This indicates that the distribution goes through a maximum only once at about spin  $5-6\hbar$ . It is assumed that the yrast band has a distribution at low angular momentum of a shape similar to that of the  $K = 0^-$  negative-parity band. The unobserved side-feeding intensities for the  $K^\pi = 2^+$  and  $2^-$  states are also plotted in Fig. 8(a) and suggest that the unobserved side-feeding distribution is indeed decreasing at  $J = 2$ .

The unobserved side-feeding intensities to the  $0^+$  and  $2^+$  yrast states,  $\Gamma$  [cf. Eq. (18)], are inferred by extrapolation (gray-shaded, open symbols, and dashed lines) in Fig. 8(b) and 100% error bars are assumed. The goal is to give a conservative estimate of the impact that  $\Gamma$  has on the  $\gamma$ -channel yield and 642 keV fraction,  $F_{\gamma\text{-ch}}(642)$ . To do this, the remaining components of  $I_{\text{tot}}(0^+)$ , Eq. (18), are measured for the same excitation energy range,  $2.6 \text{ MeV} \leq E^* \leq 6.5 \text{ MeV}$ , and they provide the following yields:  $\Sigma I_{\text{in-discrete}}(0^+) = (1.99 \pm 0.07) \times$

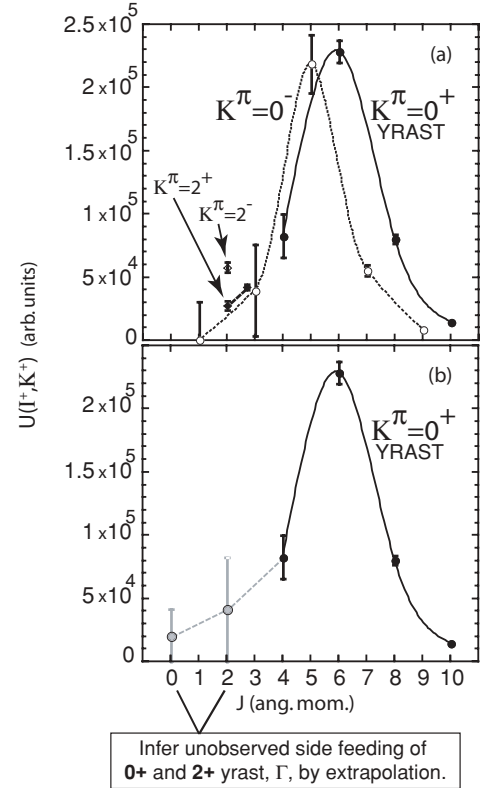


FIG. 8. (a) The unobserved side-feeding distributions for the  $K^\pi = 0^+$  yrast and  $K^\pi = 0^-$  negative-parity bands are shown ( $2.6 \text{ MeV} \leq E^* \leq 6.5 \text{ MeV}$ ). Additionally, the unobserved side feedings for the  $K^\pi = 2^+$  and  $2^-$  bands are shown to give measured quantities for  $J = 2$ . (b) The unobserved side feedings to the  $0^+$  and  $2^+$  yrast states,  $\Gamma$  (which is  $4.6 \pm 3.4\%$  of the  $\gamma$ -channel yield), are inferred by extrapolation and are given 100% error bars.

$$10^5, \Sigma I_{\text{in-discrete}}(2^+) = (1.10 \pm 0.02) \times 10^6, I(642) = (4.72 \pm 0.13) \times 10^5, \text{ and } \Gamma = (6.21 \pm 4.63) \times 10^4.$$

Finally, the 642 keV fraction [using the extrapolated value of  $\Gamma$  determined in Fig. 8(b) for  $2.6 \text{ MeV} \leq E^* \leq 6.5 \text{ MeV}$  is [E5, for example, is used below as a shorthand notation for  $( ) \times 10^5$ ]

$$\begin{aligned} F_{\gamma\text{-ch}}(642, E^* = 2.6 - 6.5 \text{ MeV}) &= \frac{I(642)}{I_{\text{tot}}(0^+)} = \frac{I(642)}{\Sigma I_{\text{in-discrete}}(0^+) + \Sigma I_{\text{in-discrete}}(2^+) + \Gamma} \\ &= \frac{4.72 \pm 0.13 E5}{1.99 \pm 0.07 E5 + 1.10 \pm 0.02 E6 + 6.21 \pm 4.63 E4} \\ &= 0.347 \pm 0.016, \end{aligned} \quad (21)$$

where  $\Gamma$  represents only  $4.6 \pm 3.4\%$  of the total  $\gamma$ -channel yield (the denominator). Therefore, the unobserved side feeding to the  $0^+$  and  $2^+$  yrast states has little effect on the  $\gamma$ -channel yield and the 642 keV fraction.

The 642 keV fraction,  $F_{\gamma\text{-ch}}(642)$ , must also be shown to be constant with excitation energy,  $E^*$ . Figure 9 shows  $F_{\gamma\text{-ch}}(642)$  as a function of excitation energy and the 642 keV fraction is indeed constant within error. To do this, narrow excitation-energy bins of 600 keV were selected using the particle data and  $F_{\gamma\text{-ch}}(642)$  was measured for each bin (it is

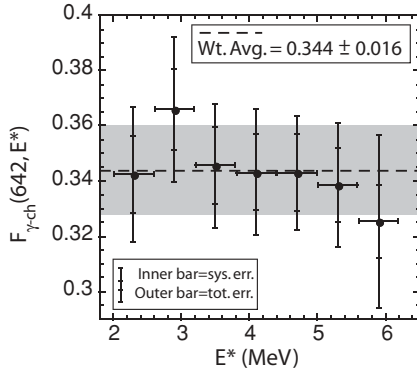


FIG. 9. The 642 keV transition fraction,  $F_{\gamma\text{-ch}}(642)$ , of the  $\gamma$ -channel yield,  $I_{\text{tot}}(0^+)$ , is shown to be constant (within error) with excitation energy,  $E^*$ .

assumed that the unobserved side feeding to the  $0^+$  and  $2^+$  yrast states,  $\Gamma$ , is a constant  $4.6 \pm 3.4\%$  of the  $\gamma$ -channel yield for all excitation energies of interest; this is a near negligible amount). Additionally, the weighted average of the 642 keV fraction,  $0.344 \pm 0.016$ , in Fig. 9 is consistent with the previous determination of  $0.347 \pm 0.016$  in Eq. (21), as it should be (i.e., they are determined over the same excitation-energy interval). The adopted value for the 642 keV fraction is

$$F_{\gamma\text{-ch}}^{\text{Adopted}}(642, E^* = 2.6 - 6.5 \text{ MeV}) = 0.347 \pm 0.016. \quad (22)$$

Preliminary Hauser-Feshbach calculations have been carried out for the decay of  $^{236}\text{U}$  by  $\gamma$  emission to see if the experimental determination of  $F_{\gamma\text{-ch}}(642)$  is in reasonable agreement with theory. The parameters for the decay model were adjusted to reproduce the  $^{235}\text{U}(n, \gamma)$  and  $^{235}\text{U}(n, f)$  cross sections. Various schematic spin distributions for the equilibrated compound nucleus,  $^{236}\text{U}$ , were considered for excitation energies between  $E^* = 2.3$  and  $7.3$  MeV (i.e.,  $E_n = -4.25$  to  $0.75$  MeV). The fraction of the  $\gamma$  cascade that proceeds through a given transition is found to be sensitive to the spin-parity distribution assumed for the compound nucleus. While it is difficult to simultaneously reproduce all relative transition intensities (suggesting, perhaps, a need for a  $K^\pi$  dependence in the model), the calculations for the various

spin distributions agree with the assumption that the 642 keV fraction of the  $\gamma$  channel is approximately independent of excitation energy. Details of these calculations will be provided elsewhere [25].

The  $^{235}\text{U}(d, p\gamma)^{236}\text{U}$   $\gamma$ -channel yield to be used in the probability ratio, Eq. (15), can now be defined as

$$\frac{N_{\gamma}^{236\text{U}}(E_n)}{\epsilon_{\gamma}} \approx \frac{I(642, E_n)}{F_{\gamma\text{-ch}}^{\text{Adopted}}(642)}, \quad (23)$$

where  $I(642, E_n)$  is the total intensity (corrected for efficiency and internal conversion) of the 642 keV transition at a given equivalent neutron energy,  $E_n = E^* - S_n$ .

## VI. ISRM RESULT AND DISCUSSION

The ISRM results, which compare the  $^{235}\text{U}(d, p\gamma)$  and  $(d, pf)$  probability ratios to the known  $^{235}\text{U}(n, \gamma)$  and  $(n, f)$  cross-section ratios [19], are given in Table I and are shown in Fig. 10. Within error, the  $^{235}\text{U}(d, p\gamma)$  and  $^{235}\text{U}(d, pf)$  surrogate reactions have  $\gamma$ -to-fission probability ratios similar to those of the neutron-induced reactions. The ISRM could be expected to perform at a similar level for neighboring nuclei. As can be seen in Fig. 10(b), the average deviation from the known cross-section ratios is 23% for  $0.9 \text{ MeV} \leq E_n \leq 3.3 \text{ MeV}$ . The errors are dominated by the statistical uncertainties in determining the  $E_{\gamma} = 642$  keV peak area. The first ISRM value at  $E_n = 0.3$  MeV is excluded from the average to avoid possible contributions from negative-neutron energies but it is shown to gauge the sensitivity to such contributions (i.e., the ISRM point at  $E_n = 0.3$  MeV is only  $\sim 1\sigma_{E^*} = 291$  keV from  $E_n < 0$  MeV and the surrogate probability ratio must approach infinity at the fission barrier,  $E_n \approx -1.55$  MeV, which is  $\sim 5.3\sigma_{E^*}$  away).

The ISRM could in principle be used to extract a host of  $(n, xn\gamma)$  cross sections relative to  $(n, f)$  if sufficient information concerning the low-lying level scheme in the residual nucleus can be experimentally obtained. This becomes more difficult to do as the number of unpaired nucleons increases and so the present method for measuring the  $\gamma$ -channel yield may be limited in practical use to even-even residual nuclei.

TABLE I. The internal surrogate ratio result: the comparison of known  $^{235}\text{U}(n, \gamma)$  and  $^{235}\text{U}(n, f)$  cross-section ratios, ENDF [19], to the  $^{235}\text{U}(d, p\gamma)$  and  $^{235}\text{U}(d, pf)$  probability ratios measured in this work.

$E_n^a \pm 0.291 \text{ MeV}$	$\gamma$ -ch yield	$f$ -ch yield	$\frac{P_{\gamma}}{P_f} = \frac{\gamma\text{-ch yield}}{f\text{-ch yield}}$	$\int \frac{\sigma(n, \gamma)}{\sigma(n, f)} \frac{dE_n}{0.6 \text{ MeV}}, [19]$	% dev.
0.3 <sup>b</sup>	$(4.49 \pm 0.52) \times 10^4$	$(1.57 \pm 0.11) \times 10^5$	$0.286 \pm 0.039$	0.201	$42 \pm 19$
0.9	$(2.06 \pm 0.34) \times 10^4$	$(1.69 \pm 0.12) \times 10^5$	$0.122 \pm 0.022$	0.101	$21 \pm 22$
1.5	$(1.19 \pm 0.31) \times 10^4$	$(2.33 \pm 0.16) \times 10^5$	$0.0511 \pm 0.0138$	0.067	$-24 \pm 21$
2.1	$(1.12 \pm 0.36) \times 10^4$	$(3.18 \pm 0.22) \times 10^5$	$0.0352 \pm 0.0116$	0.044	$-20 \pm 26$
2.7	$(7.02 \pm 3.76) \times 10^3$	$(3.62 \pm 0.25) \times 10^5$	$0.0194 \pm 0.0105$	0.0279	$-30 \pm 38$
3.3	$(5.15 \pm 4.92) \times 10^3$	$(3.72 \pm 0.26) \times 10^5$	$0.0138 \pm 0.0133$	0.0176	$-21 \pm 75$
Avg. <sup>c</sup>  dev.  $\rightarrow$ 23%					

<sup>a</sup> $E_n = E^* - S_n$ , where  $S_n = 6.55$  MeV.

<sup>b</sup>Contains a fraction of  $E_n < 0$  MeV (i.e.,  $1\sigma_{E^*} = 291$  keV).

<sup>c</sup> $E_n = 0.3$  MeV excluded.

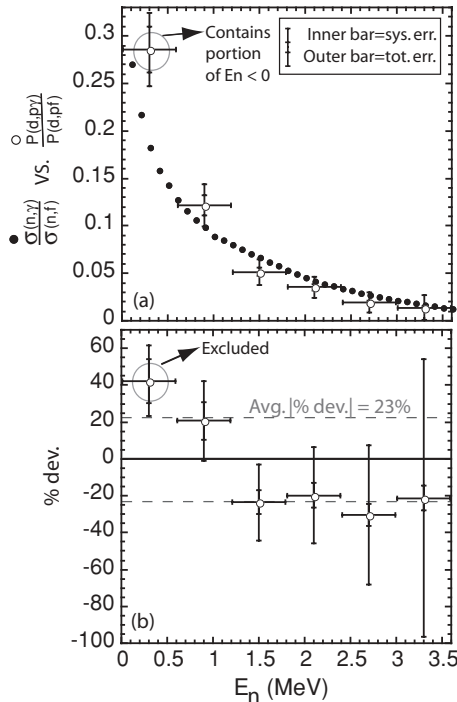


FIG. 10. (a) The comparison of known  $^{235}\text{U}(n, \gamma)$  and  $(n, f)$  cross-section ratios, ENDF [19], to the  $^{235}\text{U}(d, p\gamma)$  and  $(d, pf)$  probability ratios determined in this work. The errors are dominated by the statistical uncertainties in determining the  $E_\gamma = 642$  keV peak area. (b) The percent deviation between the known  $^{235}\text{U}(n, \gamma)$  and  $(n, f)$  cross-section ratios and  $^{235}\text{U}(d, p\gamma)$  and  $(d, pf)$  probability ratios. The average deviation is 23% for  $0.9 \text{ MeV} \leq E_n \leq 3.3 \text{ MeV}$ .

A breakdown or failure of the ISRM could be caused for either of the following reasons (possibly more):

- (i) a reaction-specific exit-channel dependence that is different for the desired and surrogate reactions (i.e., a breakdown of the Bohr compound nucleus and Weisskopf-Ewing approximation) [cf. Eq. (2) and (4)], or
- (ii) a change in the 642 keV fraction,  $F_{\gamma\text{-ch}}^{\text{Adopted}}(642)$ , for  $E^* > S_n$ , which would result in an inaccurate measure of the  $\gamma$ -channel yield (which is specific to the present method as opposed to the ISRM in general).

A study with higher particle- $\gamma$  statistics for excitation energies above  $S_n$  and/or particle-(conversion-electron) data would allow for a more sensitive test of the  $\gamma$ -channel tagging method. This would reduce the statistical uncertainties associated with the  $\gamma$ -channel measurement.

While the present study successfully shows that the ISRM is a viable option for determining relative neutron-induced cross sections, noteworthy improvements can be anticipated:

- (i) The small stopping power of protons required the use of three silicon detectors in the  $\Delta E - E$  telescope array. The third silicon detector limited the solid angle and degraded the energy resolution. Thicker

silicon detectors should be used, or the beam energy should be reduced to avoid the use of a third silicon detector.

- (ii) The limited beam time and five clover array (and limited solid angle for proton detection) reduced the particle- $\gamma$  statistics. A longer beam time ( $2.5 \rightarrow 10$  days), larger clover array ( $5 \rightarrow 7$ ), and a few low-energy  $\gamma$ -ray detectors (e.g., LEPS detectors) would greatly improve the statistics. Additionally, a larger angle coverage for the particles and an increase in  $\gamma$  statistics would allow for a direct test of energy-spin effects in the exit-channel probabilities.
- (iii) An improved reaction model for  $(d, p)$  is needed to gain physics insights.
- (iv) Background targets should be run so that the target contaminants in the particle-singles yield can be subtracted. This will allow for the determination of absolute  $\gamma$ -ray cascade probabilities and absolute cross sections.

The first two items above are estimated to increase the particle- $\gamma$  statistics by a factor of 20, which reduces the statistical uncertainties by a factor of 4. The systematic uncertainties would also be reduced (e.g., up to a twofold improvement in the particle-energy resolution).

For direct reactions with light ions, the  $\gamma$ -channel yield (with respect to the present method) may be measured most effectively by using a target nucleus with a high-spin ground state in combination with a low-angular-momentum transfer reaction. The angular momentum given to the residual nucleus from a high-spin target can reduce the unobserved side feeding to the  $0^+$  ground state. This is particularly important for actinide nuclei because the low-energy  $2^+ \rightarrow 0^+$  yrast transition is often unobserved by  $\gamma$  decay, which makes the unobserved side feeding to the  $2^+$  yrast state a concern as well. The  $J^\pi = 7/2^-$  ground-state spin of  $^{235}\text{U}$  provides the angular momentum needed to give the “turn-around” of the unobserved side-feeding distribution in Fig. 8. Without the observed peaking or “turn-around,” the unobserved side feeding to the  $0^+$  and  $2^+$  yrast states would be more difficult to extrapolate and constrain. Additionally, high-spin targets combined with low-angular-momentum transfer reactions have the benefit of minimizing the effects of anisotropy.

Future experiments are planned to continue the investigation of the surrogate reaction technique. In light of the current results, the following explorations are proposed:

- (i) Profile the unobserved side-feeding distribution as a function of excitation energy (and laboratory angle,  $\theta$ ) in small,  $\leq 0.5$  MeV, intervals for  $E_n > 0$  (this will require better energy resolution and higher statistics). Ideally this would be done for multiple reactions and target spins.
- (ii) Test the ISRM for the same compound nucleus,  $^{236}\text{U}$ , by a different reaction and with a different target spin, e.g.,  $(\alpha, \alpha')$ ,  $(^6\text{Li}, d)$ , or  $(p, t)$ .
- (iii) Test the ISRM for the  $(n, 2n\gamma)$  reaction using the same compound nucleus,  $^{236}\text{U}$ , by the same  $(d, p)$  reaction (but with a higher-energy deuteron beam).

## VII. CONCLUSIONS

The present method for measuring the  $\gamma$ -channel yield, while dependent on the feeding pattern of low-lying discrete states, does not depend on models (e.g.,  $\gamma$ -cascade calculations). This is in contrast to other methods such as the approach of Bernstein *et al.* [26]. That work obtained the total  $^{239}\text{Pu}(n, 2n\gamma)$  cross section from the use of discrete  $\gamma$ -transition yields in combination with Hauser-Feshbach and  $\gamma$ -ray cascade calculations. While Bernstein *et al.* [26] did measure the neutron-induced cross section directly, as opposed to using a surrogate reaction, the result is still dependent on model calculations. In contrast, the present approach to extracting  $(n, xn\gamma)$  cross sections is only dependent on the assumptions of the surrogate method (i.e., the Bohr compound nucleus and the Weisskopf-Ewing approximation).

The ISRM offers a valuable tool for a number of applied science areas, including, most notably, advanced fuel-cycle reactor design. Aliberti *et al.* [16] have demonstrated that  $(n, \gamma)$  cross sections on minor actinides are one of the largest sources of uncertainty in modeling new Generation-IV reactors. However, while  $(n, f)$  cross sections are relatively easy to measure, due to the strong signature provided by the

production of two high-energy fission fragments,  $(n, \gamma)$  is hard to measure (particularly for equivalent-neutron energies above 100 keV). In addition, the  $\gamma$ -to-fission ratio itself may prove to be an important quantity because it would help determine the relative fraction by which a minor actinide is burned up in a reactor by fission versus being transmuted into a heavier minor actinide by neutron capture. The ISRM offers the opportunity to determine  $(n, xn\gamma)$  cross sections with greater accuracy and to higher excitation energies.

## ACKNOWLEDGMENTS

The authors thank the 88-Inch Cyclotron operations and facilities staff for their help in performing this experiment and I. Y. Lee for useful discussions concerning the data analysis. This work was performed under the auspices of the National Science Foundation and the US Department of Energy by the University of Richmond under Grants DE-FG52-06NA26206 and DE-FG02-05ER41379, Lawrence Livermore National Laboratory under Contracts W-7405-Eng-48 and DE-AC52-07NA27344, Lawrence Berkeley National Laboratory under Contract DE-AC02-05CH11231, and Rutgers University under Contract DE-FG52-03NA00143.

- 
- [1] J. D. Cramer and H. C. Britt, Nucl. Sci. Eng. **41**, 177 (1970).  
 [2] W. Younes and H. C. Britt, Phys. Rev. C **67**, 024610 (2003); W. Younes and H. C. Britt, Phys. Rev. C **68**, 034610 (2003).  
 [3] M. Petit, M. Aiche, G. Barreau, S. Boyer, N. Carjan, S. Czajkowski, D. Dassie, C. Grosejean, A. Guiral, B. Haas *et al.*, Nucl. Phys. **A735**, 345 (2004).  
 [4] C. Plettner, H. Ai, C. W. Beausang, L. A. Bernstein, L. Ahle, H. Amro, M. Babilon, J. T. Harke, J. A. Caggiano, R. F. Casten *et al.*, Phys. Rev. C **71**, 051602(R) (2005).  
 [5] J. E. Escher and F. S. Dietrich, Phys. Rev. C **74**, 054601 (2006).  
 [6] J. T. Harke, L. A. Bernstein, J. E. Escher, L. Ahle, J. A. Church, F. S. Dietrich, K. J. Moody, E. B. Norman, L. Phair, P. Fallon *et al.*, Phys. Rev. C **73**, 054604 (2006).  
 [7] S. Boyer, D. Dassié, J. N. Wilson, M. Aiche, G. Barreau, S. Czajkowski, C. Grosjean, A. Guiral, B. Haas, B. Osmanov *et al.*, Nucl. Phys. **A775**, 175 (2006).  
 [8] B. F. Lyles, L. A. Bernstein, J. T. Harke, F. S. Dietrich, J. E. Escher, I. Thompson, D. L. Bleuel, R. M. Clark, P. Fallon, J. Gibelin *et al.*, Phys. Rev. C **76**, 014606 (2007).  
 [9] B. L. Goldblum, S. G. Prussin, U. Agvaanluvsan, L. A. Bernstein, D. L. Bleuel, W. Younes, and M. Guttormsen, Phys. Rev. C **78**, 064606 (2008).  
 [10] B. K. Nayak, A. Saxena, D. C. Biswas, E. T. Mirgule, B. V. John, S. Santra, R. P. Vind, R. K. Choudhury, and S. Ganesan, Phys. Rev. C **78**, 061602(R) (2008).  
 [11] S. R. Leshner, J. T. Harke, L. A. Bernstein, H. Ai, C. W. Beausang, D. L. Bleuel, R. M. Clark, F. S. Dietrich, J. E. Escher, P. Fallon *et al.*, Phys. Rev. C **79**, 044609 (2009).  
 [12] R. Hatarik, L. A. Bernstein, J. T. Burke, J. A. Cizewski, J. D. Gibelin, S. R. Leshner, P. D. O'Malley, L. W. Phair, and T. Swan, AIP Conf. Proc. **1005**, 105 (2008).  
 [13] N. D. Scielzo, L. A. Bernstein, D. L. Bleuel, J. T. Burke, S. R. Leshner, E. B. Norman, S. A. Sheets, M. S. Basunia, R. M. Clark, P. Fallon *et al.*, AIP Conf. Proc. **1005**, 109 (2008).  
 [14] N. Bohr, Nature (London) **137**, 344 (1936).  
 [15] S. N. Ghoshal, Phys. Rev. **80**, 939 (1950).  
 [16] G. Aliberti, G. Palmiotti, M. Salvatores, and C. G. Stenberg, Nucl. Sci. Eng. **146**, 13 (2004); G. Aliberti, G. Palmiotti, M. Salvatores, T. K. Kim, T. A. Taiwo, M. Anitescu, I. Kodeli, E. Sartori, J. C. Bosq, and J. Tommasi, Ann. Nucl. Energy **33**, 700 (2006).  
 [17] H. C. Britt and J. B. Wilhelmy, Nucl. Sci. Eng. **72**, 222 (1979).  
 [18] V. F. Weisskopf and D. H. Ewing, Phys. Rev. **57**, 472 (1940).  
 [19] M. B. Chadwick, P. Obložinský, M. Herman, N. M. Greene, R. D. McKnight, D. L. Smith, P. G. Young, R. E. MacFarlane, G. M. Hale, S. C. Frankle *et al.*, Nucl. Data Sheets **107**, 2931 (2006).  
 [20] G. Duchêne, F. A. Beck, P. J. Twin, G. de France, D. Curien, L. Hana, C. W. Beausang, M. A. Bentley, P. J. Nolan, and J. Simpson, Nucl. Instrum. Methods Phys. Res. A **432**, 90 (1999); Z. Elekes, T. Belgya, G. L. Molnár, A. Z. Kiss, M. Csatlós, J. Gulyás, A. Krasznahorkay, and Z. Máté, Nucl. Instrum. Methods Phys. Res. A **503**, 580 (2003).  
 [21] R. Vandenbosch, K. L. Wolf, J. Unik, C. Stephan, and J. R. Huizenga, Phys. Rev. Lett. **19**, 1138 (1967).  
 [22] H. J. Specht, J. S. Fraser, and J. C. Milton, Phys. Rev. Lett. **17**, 1187 (1966).  
 [23] H. C. Britt, F. A. Rickey, Jr., and W. S. Hall, Phys. Rev. **175**, 1525 (1968).  
 [24] E. Browne and J. K. Tuli, Nucl. Data Sheets **107**, 2649 (2006); E. Browne, Nucl. Data Sheets **98**, 665 (2003).  
 [25] J. E. Escher *et al.* (to be published).  
 [26] L. A. Bernstein, J. A. Becker, P. E. Garrett, W. Younes, D. P. McNabb, D.E., Archer, C. A. McGrath, H. Chen, W. E. Ormand, M. A. Stoyer *et al.*, Phys. Rev. C **65**, 021601(R) (2002).